https://doi.org/10.5194/egusphere-2026-4199
Preprint. Discussion started: 22 July 2026

Past and future projected radiative effects from irrigation

Amen Al-Yaari[1], Chris Smith[2], Yi Yao[3], Kjetil Schanke Aas[4], L. Ruby Leung[5], Min-Hui Lo[6], Sonali McDermid[7], Larissa Nazarenko[8], Yadu Pokhrel[9], Yusuke Satoh[10], Tokuta Yokohata[11], and Wim Thiery[1]

[1]Department of Water and Climate, Vrije Universiteit Brussel, Brussels, Belgium
[2]Energy, Climate and Environment Program, International Institute for Applied Systems Analysis (IIASA), Laxenburg, Austria
[3]Institute for Atmospheric and Climate Science, Department of Environmental Systems Science, ETH Zurich, Zurich, Switzerland
[4]CICERO - Center for International Climate Research, Oslo, Norway
[5]Atmospheric, Climate, and Earth Sciences Division, Pacific Northwest National Laboratory, Richland, WA, USA
[6]Department of Atmospheric Sciences, National Taiwan University, Taipei, Taiwan
[7] Department of Environmental Studies, New York University, New York, NY, USA
[8]NASA Goddard Institute for Space Studies, New York, NY 10025, USA
[9]Department of Civil and Environmental Engineering, Michigan State University, East Lansing, MI, USA
[10]Japan Agency for Marine-Earth Science and Technology, Yokohama, Japan
[11]National Institute for Environmental Studies, Tsukuba, Japan

Correspondence to: Amen Al-Yaari (amen.al.yaari@vub.be)

Abstract. Irrigation is the most dominant freshwater-use practice on Earth, yet its effect on the top of atmosphere (TOA) radiative budget remains highly uncertain because past estimates have relied on idealised experiments or single-model frameworks. Here we capitalise on the Irrigation Model Intercomparison Project (IRRMIP) to provide the first multi-model quantification of irrigation-induced effective radiative forcing (ERF), defined here as the change in net TOA radiative flux including rapid atmospheric adjustments under prescribed sea surface temperatures (SST), over the historical period (1902-2014). Across seven Earth system models, under fixed SST conditions, the global multi-model mean (MMM) irrigation-induced ERF is positive but small (~ 0.023 W m^{-2}), reflecting a near-cancellation between the positive longwave contribution associated with irrigation-induced atmospheric moistening and the negative shortwave contribution associated with enhanced reflection, including cloud-related effects. While the global signal is small, it masks pronounced regional heterogeneity: South Asia and West Central Asia exhibit substantially higher positive ERF (~ 0.25 W m^{-2}), with spatial maps revealing coherent forcing hotspots of up to +5 W m^{-2} over the Indo-Gangetic Plain that are consistent across all models, while East Asia shows a persistent negative signal (-0.03 W m^{-2}). The clear-sky ERF is greater than the all-sky ERF in most regions, indicating that cloud adjustments following irrigation exert a systematic negative contribution to the ERF. We additionally examine future changes in net TOA radiation imbalance ($\Delta R_{n,TOA}$) from a fully coupled CMIP-style model (SSP1-2.6 and SSP3-7.0, 2015-2070) to assess whether the historical ERF pattern persists under future irrigation. A more global positive $\Delta R_{n,TOA}$ is found under the high-irrigation-demand SSP3-7.0 pathway relative to SSP1-2.6, consistent with

https://doi.org/10.5194/egusphere-2026-4199
Preprint. Discussion started: 22 July 2026

projected differences in irrigation expansion between scenarios. Correlations between historical ERF variability and its potential drivers suggest that reduced outgoing longwave radiation is the dominant control at the global scale and in South Asia and West Central Asia, while near-surface temperature, precipitable water, albedo, and cloud cover contribute with substantial regional and inter-model variability. These results demonstrate that irrigation's radiative influence, while small in the global mean, is regionally substantial and scenario-dependent, with implications for the attribution of regional climate change and for the design of land-based mitigation trajectories.

1 Introduction

Irrigation is the most dominant freshwater-use practice globally, supporting 40% of the world's food supply (Siebert et al., 2015) and accounting ~70% of total human freshwater withdrawals (Döll et al., 2009; Siebert et al., 2010) and ~ 90% of consumptive water (Siebert et al., 2010). Since 1901, the area equipped for irrigation (AEI) has expanded more than fivefold, reaching approximately 3 million km^2 by 2014 (Hurtt et al., 2020a; McDermid et al., 2023). This massive expansion has profound impacts on the Earth system (Mahmood et al., 2014; Roy et al., 2007; Tuinenburg et al., 2011), altering global and regional water cycles (Puma and Cook, 2010; Wu et al., 2022), energy balances (Al-Yaari et al., 2022; Thiery et al., 2017), heat extremes (Mishra et al., 2020; Thiery et al., 2020; Yao et al., 2025a), and biogeochemical fluxes (Boucher et al., 2004). The primary biophysical effect is evaporative cooling, where irrigation water shifts the surface energy partition by increasing latent heat flux relative to sensible heat flux (Cook et al., 2015; Li et al., 2026; Mueller et al., 2017; Seneviratne et al., 2010).

At the Earth system scale, the evaporation of irrigation water introduces contrasting thermodynamic effects by adding additional moisture into the atmosphere. As a greenhouse gas, this water vapor traps outgoing longwave radiation, potentially exerting a positive radiative forcing, while its eventual condensation releases latent heat directly into the atmosphere (Koll and Cronin, 2018). Consequently, irrigation alters the vertical temperature profile by cooling the surface via the latent heat flux while simultaneously warming the mid-to-upper troposphere (Boucher et al., 2004). Radiative forcing describes the total imposed energy on the climate system and can be used to predict long-term climate responses, offering insight into the key drivers of climate change (Sharma et al., 2026). A positive radiative forcing (RF) means a net energy gain that would exert a warming influence on the Earth's climate system, whereas a negative RF signifies a net energy loss, inducing a cooling effect (Bellouin et al., 2020; Forster et al., 2016). Boucher et al. (2004) estimated global mean RF from irrigation-induced water vapor of about +0.03 to +0.1 W/m² in idealized simulations (i.e., a prescribed-vapor simulations). However, the authors found a decrease in surface temperature dominated by evaporative cooling rather than by the excess greenhouse effect. Cook et al. (2015) found that RF at the TOA is about 0.02 W/m² using GISS ModelE2 (compared to a non-irrigated control baseline scenario).

https://doi.org/10.5194/egusphere-2026-4199
Preprint. Discussion started: 22 July 2026

The traditional stratospherically-adjusted RF metric is poorly suited for assessing near-surface water vapor perturbations in climate models because it requires the tropospheric state to remain fixed (IPCC, 2014). As a result, tropospheric radiative adjustments, which have been shown to play an important role in the response to irrigation forcing (Sherwood et al., 2018), are not accounted for (Sherwood et al., 2015). Effective RF (ERF) is a better predictor of long-term temperature change than RF (Ramaswamy et al., 2018) and is the recommended method to assess the radiative impacts of climate perturbations (IPCC, 2023). Instantaneous radiative forcing refers to the immediate radiative effect of an imposed perturbation before the atmospheric and land-surface state adjusts. Rapid adjustments include subsequent changes in clouds, atmospheric temperature and humidity profiles, and land-surface conditions that occur without an SST-mediated climate response; ERF includes both contributions. Until now, global estimates of irrigation-induced ERF still rely on a limited number of modelling frameworks or single-model studies (e.g., Boucher et al., 2004; Gormley-Gallagher et al., 2022; Sherwood et al., 2018). Consequently, the global-scale magnitude of irrigation-driven greenhouse forcing remains highly uncertain (Li et al., 2022).

Using the Community Earth System Model (CESM 1.2.2), Sherwood et al. (2018) found that irrigation-emitted water vapor has a very low Global Warming Potential (GWP), with total global ERF equal to -0.026 W/m², opposite in sign to what is expected from an increased water vapour greenhouse effect. This was explained by the negative rapid adjustments due to an increase in low cloud amount, and because the increased moisture rains out before reaching radiatively sensitive altitudes. Using the same model and a mechanistic irrigation parameterisation, Gormley-Gallagher et al. (2022) found that irrigation-induced ERF at the TOA is about 0.05 W/m². While these studies offered new insights into irrigation-induced ERF, they were restricted to single-model perspectives and used a diversity of modelling approaches to estimate irrigation ERF, challenging disentangling structural model uncertainties from uncertainties in the water vapour flow to the atmosphere.

To address these structural uncertainties and consolidate our understanding of irrigation-climate interactions, the Irrigation Model Intercomparison Project (IRRMIP) was established (Yao et al., 2025a, 2025c). IRRMIP provides a multi-model framework involving state-of-the-art Earth System Models (ESMs), including CESM2, CESM2-groundwater (CESM2_GW; a variant incorporating a groundwater parameterisation), CNRM-CM6-1 (CNRM), E3SMv2 (E3SM), MIROC-INTEG-ES (MIROC), NASA GISS climate model (NASA-GISS), NorESM2 (NorESM), and IPSL-CM6, to simulate the impacts of transient irrigation expansion from 1902 to 2014. Although IRRMIP has already been used to assess the thermal and hydrological impacts of irrigation, its multi-model ensemble has not yet been used to quantify irrigation-induced ERF. Initial IRRMIP results led by Yao et al. (2025a) have demonstrated that while irrigation reduces dry-heat extremes, it can amplify moist-heat stress and aggravate land water depletion (Yao et al., 2025c), emphasizing the complex trade-offs of irrigation as an adaptation strategy. In this study, we leverage the IRRMIP multi-model ensemble to provide the first comprehensive quantification of irrigation-induced ERF across multiple model structures. Furthermore, we extend the analysis beyond historical simulations (1902-2014) to available future projections in one model under two Shared Socio-economic Pathways (SSPs), namely SSP1-2.6 and SSP3-7.0, which incorporate transient changes in both irrigation extent and efficiency.

https://doi.org/10.5194/egusphere-2026-4199
Preprint. Discussion started: 22 July 2026

Because these future simulations are fully coupled (CMIP-style), in contrast to the fixed-SST (AMIP-style) historical IRRMIP experiments, note that the corresponding radiative quantity reflects both irrigation forcing and the radiative consequences of the coupled SST and circulation response and is reported here as the net TOA radiation imbalance ($\Delta R_{n,TOA}$) rather than ERF (see Section 2.2). We use this future $\Delta R_{n,TOA}$ not as a direct extension of the historical ERF time series, but as an independent test of whether the regional forcing pattern identified historically persists or intensifies under future irrigation and socioeconomic scenarios. This represents a critical gap given that future irrigation demand is projected to change under both climate warming and evolving agricultural practices. To this end, this study addresses three objectives:

I. Quantifying the historical irrigation-induced ERF (1902-2014) across seven IRRMIP models and characterising its spatial structure and inter-model spread;

II. Identifying the dominant physical drivers of historical irrigation ERF, by analysing the relationship between ERF and key atmospheric and surface variables: total, high, medium, and low cloud cover, surface albedo, near-surface temperature, upwelling and downwelling shortwave and longwave radiation, and precipitable water; and

III. Assessing the projected future $\Delta R_{n,TOA}$ radiation imbalance (2015-2070) under SSP1-2.6 and SSP3-7.0 to evaluate whether the regional pattern of irrigation forcing identified historically strengthens or weakens under different socioeconomic and emission trajectories.

2 Methods

2.1 The IRRMIP framework

The IRRMIP protocol consists of two transient atmosphere-land experiments with prescribed SST and sea ice (AMIP-style) over 1901–2014: one with and one without irrigation expansion (Yao et al., 2025a). Here, we analyse simulations from seven models: CESM2, CESM2_GW, MIROC, CNRM, NorESM, NASA-GISS, and E3SM. The irrigated experiment (IRR) prescribes the transient historical evolution of irrigation extent and applies dynamically computed irrigation amounts to the land surface, whereas the no-irrigation-expansion control (NOI) uses identical boundary conditions but maintains irrigation conditions at their 1901 levels. The difference between the two experiments isolates the climate response to irrigation expansion, with SST and sea ice prescribed in both simulations. Irrigation represented in the models can be grouped into two categories: external forcing applications (only for CNRM and NASA-GISS) and soil-moisture-based schemes. Soil-moisture-based irrigation modules and their characteristics (irrigation triggers, start time, amount, etc.) are different among models. It should be noted that although CESM2, CESM2_GW, and NorESM share similar land system models, they differ in atmospheric models and features in the irrigation scheme. The reader is kindly directed to Yao et al. (2025a) for more detailed descriptions of the models and their irrigation schemes. Multiple ensemble members are used per model where available (five for CNRM and NASA-GISS, two for NorESM and E3SM, three for MIROC, CESM2_GW and CESM2), and the per-model ensemble mean is computed before deriving the multi-model mean.

https://doi.org/10.5194/egusphere-2026-4199
Preprint. Discussion started: 22 July 2026

In Yao et al. (2025b), future irrigation projections were modelled by developing dynamic irrigation efficiency and extent scenarios explicitly tied to the SSPs, thereby moving away from the static, present-day irrigation baselines used in previous studies. To project future irrigation, the authors developed a new dataset of Irrigation Techniques Share (ITS) aligned with two contrasting SSPs: SSP1-2.6 (a sustainable "green road" with low mitigation and adaptation challenges) and SSP3-7.0 (a "rocky road" with high challenges for both). These scenarios capture the real-world transition from traditional, highly consumptive flood irrigation to modern water-saving techniques like drip and sprinkler systems. Future changes in irrigation extent were taken from the Land Use Harmonization version 2 (LUH2) dataset, while the transition between irrigation methods, drip, sprinkler, and flood, was projected using a hydro-economic framework that classifies countries based on socioeconomic indicators (GDP, governance, urbanisation, gender inequality) and hydroclimatic conditions (precipitation), assuming that wealthier and drier countries adopt efficient techniques faster. These transient ITS scenarios were then implemented in CESM2, which was extended to allow multiple irrigation techniques per crop type per grid cell, enabling yearly updates to the mix of irrigation methods (Yao et al., 2022). Fully coupled climate simulations were run from 2015 to 2074 under both scenarios, each with three ensemble members, with and without irrigation, to isolate the climate impacts of irrigation from those of greenhouse gas forcing.

2.2 Computation of ERF

At the top of the model, net downward radiation is defined as FSNT - FLNT, where FSNT is net shortwave radiation taken as positive downward and FLNT is net longwave radiation taken as positive upward. The irrigation-induced change in net TOA radiation is therefore calculated as the difference between the IRR and NOI experiments: ERF is the sum of the instantaneous radiative forcing and its rapid adjustments, which act on atmospheric timescales and affect the vertical distribution of temperature and moisture, and thus cloud formation. The irrigation-induced ERF is computed at the top of the model as:

$$\Delta ERF = (FSNT_{IRR} - FLNT_{IRR}) - (FSNT_{NOI} - FLNT_{NOI}) \qquad (1)$$

Because SST and sea ice are prescribed in the historical experiment, this net TOA radiation difference is interpreted as ΔERF, which comprises the instantaneous radiative effect of the imposed perturbation and the associated rapid adjustments. For each model, ΔERF is computed per ensemble member and then averaged across members. Note that CNRM does not provide FSNT and FLNT directly but instead provides the CMIP standard-name variables rsdt (shortwave downward radiation at TOA), rsut (shortwave upward radiation at TOA), and rlut (longwave upward radiation at TOA); for this model, FSNT was computed as rsdt - rsut and FLNT was assumed equal to rlut.

https://doi.org/10.5194/egusphere-2026-4199
Preprint. Discussion started: 22 July 2026

This ΔERF computation is valid for the historical AMIP-style simulations, where SST and sea ice are prescribed, as already mentioned. The future scenario simulations (CESM2 SSP1-2.6 and SSP3-7.0) are fully coupled, allowing SST to respond to the irrigation perturbation; the same IRR-NOIRR difference in net TOA radiation in this configuration reflects forcing together with the radiative consequences of the coupled climate response, rather than ΔERF in the strict sense. We therefore report this future-period quantity as the net TOA radiation imbalance ($\mathbf{\Delta R_{n,TOA}}$) rather than ΔERF.
The multi-model mean (MMM) ΔERF is computed by averaging each model's ensemble-mean ΔERF over 1902-2014. For the spatial maps of historical ΔERF (Fig. 3), the period (1981-2014) mean is shown on a common grid, regridded using linear interpolation to the CESM2 grid. For the future spatial maps (Fig. 7), the 2050-2070 mean is used, following the analysis period adopted by Yao et al. (2025b). A 21-year, first-degree Savitzky-Golay smoothing filter (Savitzky and Golay, 1964) is applied to all time series prior to display (Figs.1-2,4-5), to highlight decadal-to-multidecadal variability while suppressing interannual noise. Finally, only five models, CNRM, CESM2_GW, MIROC, NASA-GISS, and E3SM, provide more variables beyond FSNT and FLNT, allowing the computation of clear-sky ΔERF and assessment of potential physical drivers of ΔERF.

3 Results and Discussion

3.1 Regional and global historical annual mean ERF

At the global scale, the irrigation-induced all-sky ΔERF remains small throughout the entire period (Fig. 1A), with the multi-model mean, reported in Table 1, being about +0.023 W m^{-2}. This small magnitude may reflect the compensation between the longwave and shortwave components of the irrigation ΔERF (Boucher et al., 2004). The direction of the global mean ΔERF is consistent with previous studies (e.g., Boucher et al., 2004; Cook et al., 2015; Gormley-Gallagher et al., 2022), though the magnitudes are not identical, but opposite in sign to Sherwood et al. (2018). Sherwood et al. (2018) and Gormley-Gallagher et al. (2022) reported opposite irrigation impacts on ΔERF. However, the perturbations considered in the two studies are not directly comparable. Sherwood et al. imposed an idealized near-surface water-vapour source without accounting for the associated surface evaporative cooling, whereas Gormley-Gallagher et al. represented irrigation interactively through the land model.

https://doi.org/10.5194/egusphere-2026-4199
Preprint. Discussion started: 22 July 2026

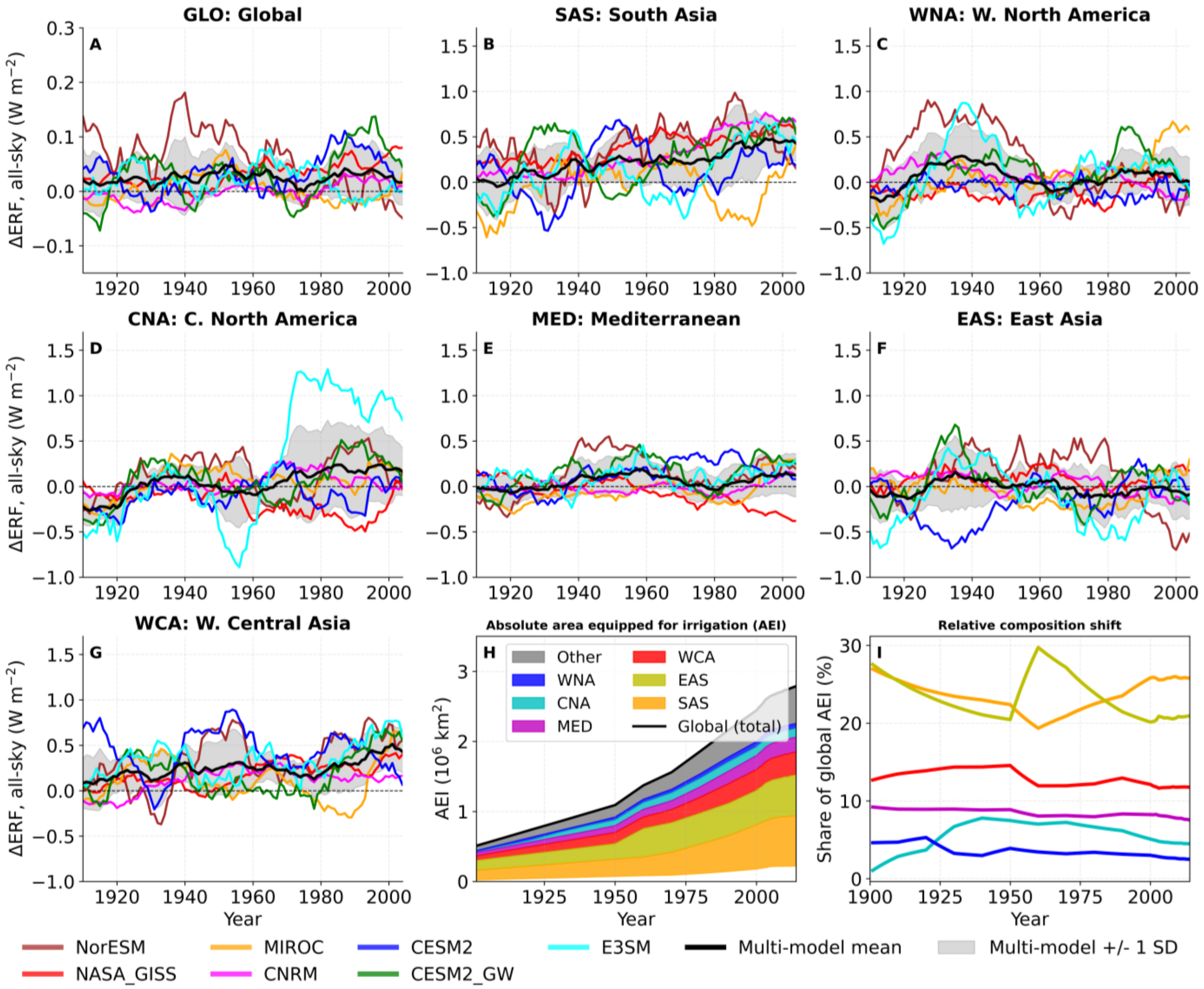

Figure 1: (A-G) Global and regional annual mean all-sky ΔERF (W m⁻²) from irrigation for each model and the multi-model mean (black line), for the historical period (1902-2014). A 21-year Savitzky-Golay smoother is applied. Shading indicates inter-model spread (±1 standard deviation). (H) Global and regional time series of area equipped for irrigation (AEI) in 1901-2014. (I) Relative composition shift in regional contributions to global AEI, expressed as the share (%) of each region's irrigated area relative to the global total over 1901-2014, illustrating how the regional balance of irrigation expansion has changed over time. To minimize edge effects introduced by the 21-year Savitzky-Golay filter, the first and last 10 years of the record are not shown. The area equipped for irrigation data is from the Land-Use Harmonization phase 2 (LUH2) project (Hurtt et al., 2020b). The spatial extent of the regions is shown in Fig. 3A.

https://doi.org/10.5194/egusphere-2026-4199
Preprint. Discussion started: 22 July 2026

Regionally (see Fig.3A for the regions boundaries), the historical ΔERF time series under all-sky conditions show a gradual intensification of the irrigation signal through the 20th century, broadly tracking the global expansion of irrigated area (Figs.1 B, H). Irrigation rapidly expanded during the 20th century, leading to a progressive modification of the atmospheric column above irrigated regions (Yao et al., 2025a). The rate of ΔERF change accelerates after approximately 1950, consistent with the rapid post-war expansion of irrigation infrastructure in Asia. South Asia (SAS; Fig.1 B) shows the strongest and most coherent positive ΔERF signal, rising progressively from near zero in the early 20th century to values approaching 0.5 W m^{-2} by the 1980s for NorESM, with a historical multi-model mean of +0.22 W m^{-2}. This is consistent with the massive expansion of irrigated area in the Indian subcontinent, as evident in Fig.1 I: SAS evolved from contributing a modest share of global irrigated area to dominating it by the early 21st century. The large positive ΔERF (i.e., warming influence) here may reflect reduced TOA outgoing longwave from increased atmospheric moisture, outweighing shortwave cloud effects, a pattern noted for northern India in earlier single-model studies (Cook et al., 2015). West Central Asia (WCA; Fig.1 G) displays a similarly rising positive historical ΔERF mean of +0.24 W m^{-2}, associated with extensive irrigation in Central Asian river basins. The Mediterranean (MED; Fig.1 E) region shows weaker ΔERF (+0.05 W m^{-2}) but is rather stable over time. Western North America (WNA; Fig.1 C), Central North America (CNA; Fig.1 D) and East Asia (EAS; Fig.1 F) show a smaller ΔERF. Overall, while the global ΔERF from irrigation is small, the regional ΔERF can reach magnitudes of 0.4 W m^{-2} in SAS and WCA, comparable to the magnitude of aerosol ERF signals in South Asia (Sharma et al., 2026). This has implications for detection and attribution: irrigation and aerosol forcing may partially co-vary in time and space in heavily industrialised and irrigated regions, making their separation in observational records challenging (van Oldenborgh et al., 2018).

https://doi.org/10.5194/egusphere-2026-4199
Preprint. Discussion started: 22 July 2026

Table 1: Period-mean ΔERF (historical, AMIP) and $\Delta R_{n,TOA}$ (future scenarios, coupled CMIP) from irrigation (IRR minus NOIRR) in W m^{-2}, derived from annual means. Historical simulations cover 1902-2014; future SSP scenarios cover 2015-2070. Multi-model mean (MMM) and 95% confidence interval (t-distribution) are shown. Regions: GLO = Global; SAS = South Asia; WNA = W. North America; CNA = C. North America; MED = Mediterranean; EAS = East Asia; WCA = W. Central Asia. Note: historical ΔERF and future $\Delta R_{n,TOA}$ are not directly comparable in magnitude, owing to differing experimental design (fixed-SST AMIP-style vs. fully coupled CMIP-style simulations, Section 2.2); comparisons between the two blocks should be limited to spatial/regional patterns, not absolute values.

Model	Global	South Asia	W. North America	C. North America	Mediterranean	East Asia	W. Central Asia
Historical period mean ΔERF (W m^{-2}; 1902-2014)							
NASA_GISS	0.039	0.396	-0.111	-0.136	-0.081	0.068	0.185
MIROC	0.006	-0.017	0.115	0.059	-0.020	-0.011	0.165
CESM2	0.028	0.113	-0.056	-0.062	0.133	-0.150	0.425
CNRM	-0.004	0.320	0.056	0.026	-0.008	0.011	0.110
E3SM	0.018	0.134	-0.011	0.206	0.111	-0.173	0.353
NorESM	0.047	0.340	0.171	0.076	0.110	0.023	0.279
CESM2_GW	0.025	0.281	0.023	0.015	0.136	0.012	0.182
MMM Mean	**0.023**	**0.224**	**0.027**	**0.026**	**0.054**	**-0.031**	**0.243**
MMM ±95% CI	**±0.016**	**±0.138**	**±0.090**	**±0.100**	**±0.082**	**±0.085**	**±0.105**
Future scenario period mean $\Delta R_{n,TOA}$ (W m^{-2}; 2015-2070)							
CESM2_SSP3-7.0	0.022	1.593	0.336	0.255	0.293	-0.234	0.868
CESM2_SSP1-2.6	-0.014	1.322	-0.052	0.069	0.021	-0.193	0.988

When repeating the same analysis under clear-sky conditions, a more pronounced ΔERF signal emerges across all regions (Fig. 2). Globally, the clear-sky forcing exhibits a systematic upward trajectory, particularly after the mid-20th century. This amplification, also true over SAS, MED, WCA, and CNA, when moving from all-sky to clear-sky diagnostics, indicates the presence of a negative cloud radiative adjustment operating within the multi-model ensemble. This may suggest that irrigation-induced cloud changes partially offset the positive clear-sky water-vapor radiative effect. Such a negative adjustment may arise from enhanced cloud reflection and increased planetary albedo, leading to a cooling effect, or from changes in cloud distributions associated with enhanced surface evaporation and latent heat flux, which can modify atmospheric stability and cloud formation. In particular, increased partitioning of available energy into latent rather than sensible heat flux may reduce boundary-layer warming and potentially affect low-cloud development, further contributing to the overall cloud-mediated cooling response. In South and West Central Asia, clouds appear to damp an otherwise positive clear-sky ERF, whereas in East Asia the clear-sky signal is weakly positive or near zero while the all-sky signal is negative,

https://doi.org/10.5194/egusphere-2026-4199
Preprint. Discussion started: 22 July 2026

suggesting that cloud-associated effects may determine or even reverse the sign of the regional ERF. The response appears less robust and more model dependent over North America and the Mediterranean.

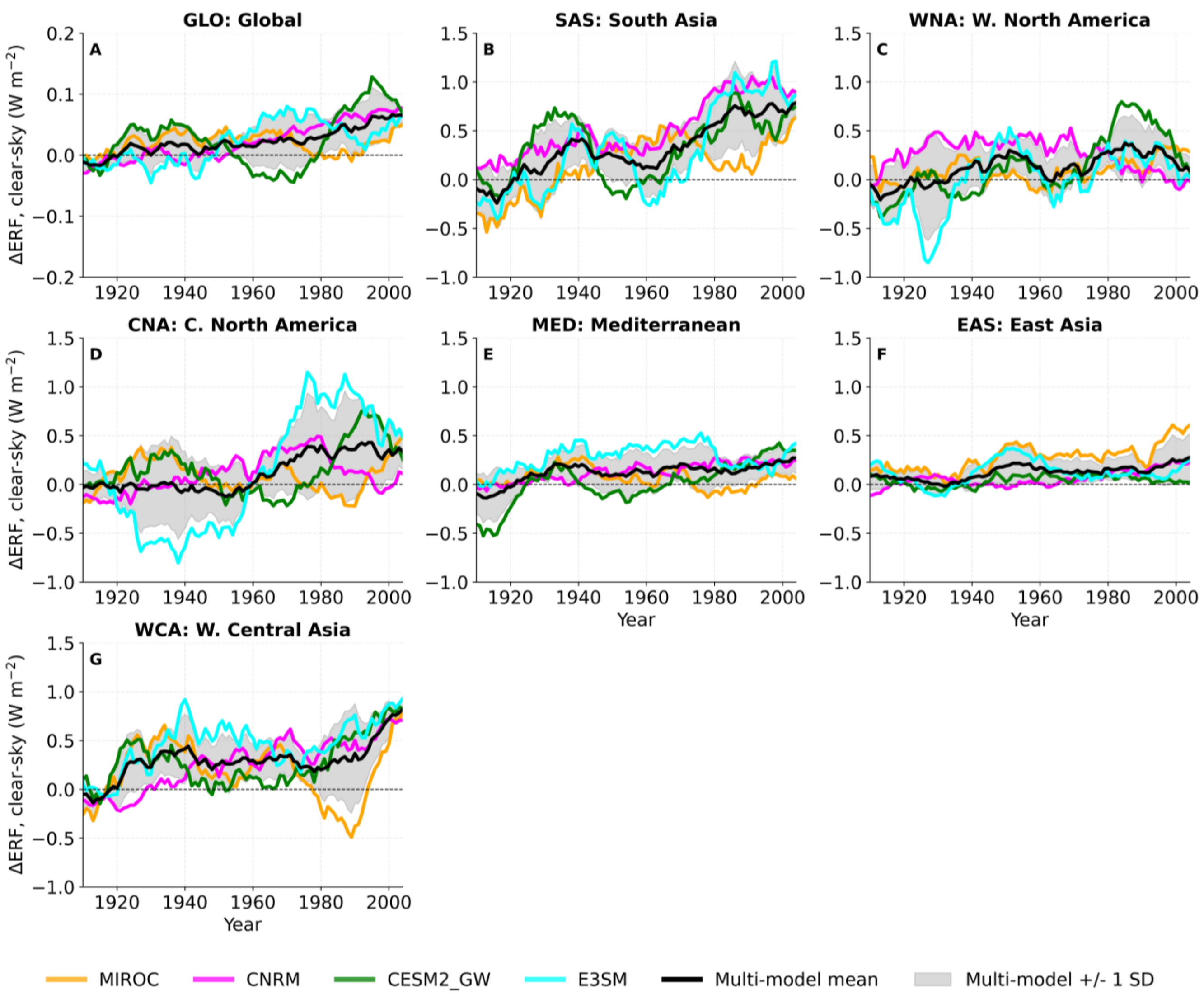

Figure 2: same as Fig.1 but under clear-sky conditions and for only the models that provide FSNTC and FLNTC. To minimize edge effects introduced by the 21-year Savitzky-Golay filter, the first and last 10 years of the record are not shown.

Furthermore, we present the spatial distribution of the historical (1981-2014) annual mean irrigation-induced ΔERF across individual models (Fig.3 A-G), and the multi-model mean (Fig. 3H). The spatial maps reveal that while the global mean ΔERF remains small, irrigation imposes strong, highly localized radiative signatures that are concentrated over major agricultural basins. The spatial structure confirms why SAS and WCA dominate the regional time-series signals. A spatially

https://doi.org/10.5194/egusphere-2026-4199
Preprint. Discussion started: 22 July 2026

coherent positive ΔERF hotspot (+ 2 to +5 W m^{-2}) stretches across northern India and Pakistan, a feature that is replicated across all models. This intense positive patch explains the increase in the SAS region seen after 1950 in Fig 2, confirming that the addition of atmospheric moisture across the Indian subcontinent acts locally as a massive longwave greenhouse trap. Strong positive forcing regions (+1 to +3 W m^{-2}) are clustered around the Aral Sea basin and adjacent river valleys in West Central Asia. This footprint anchors the upward historical trajectory tracked in the WCA time-series (Figs 1G and 2G). Over Eastern and Central China, the models display a negative forcing signature (-1 to -3 W m-2), especially in NorESM and E3SM. This regional cooling explains the small downward trend noted in the EAS time series (Table 1). The models exhibit strong patches of warming over the Mississippi basin. Hatched areas (Fig. 3H), where ≥80% of models agree on sign of change and |MMM| > 1 W/m^2, over the Indo-Gangetic Plain confirm that the regional intensification captured throughout the 20th-century time series is a coherent climate response across independent modelling frameworks. The spatial co-location of these positive and negative anomalies explains the global-scale buffering effect, showing that the near-zero global mean ERF is not an indication of weak thermodynamic activity, but rather the result of distinct regional forcing patterns counterbalancing one another.

https://doi.org/10.5194/egusphere-2026-4199
Preprint. Discussion started: 22 July 2026

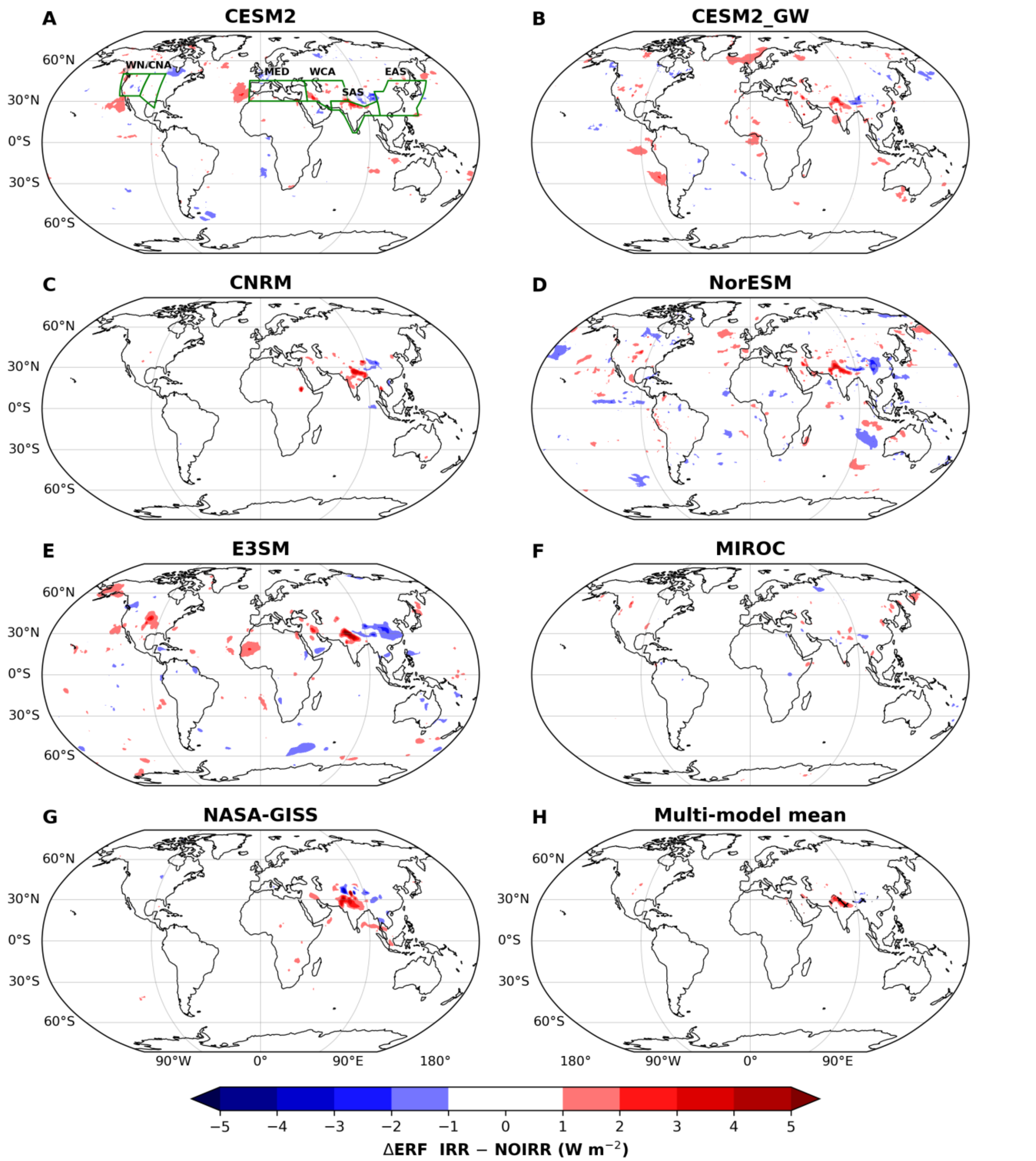

270 **Figure 3:** Global maps of the 1981-2014 mean effective radiative forcing from irrigation (ΔERF; W m⁻²) for each of the seven IRRMIP models (CESM2, CESM2-GW, CNRM, NorESM, NASA-GISS, MIROC, and E3SM) and their multi-model mean. Hatches mark areas where the 80% of the models agree on the sign.

https://doi.org/10.5194/egusphere-2026-4199
Preprint. Discussion started: 22 July 2026

3.2 Physical drivers and feedback mechanisms

To uncover the physical processes governing the coupling between irrigation and historical ΔERF, we examine the co-variation of ΔERF with a suite of land and atmospheric variables for only the five models (CNRM, CESM-GW, MIROC, NASA-GISS, and E3SM) that provide variables beyond FSNT and FLNT to diagnose the physical drivers of ΔERF. Following the definition of ΔERF (eq. 1), we analyse inter-model correlations across various regions (Fig. 4). Figure 4 displays the correlations over 1910-2004 between ΔERF and total cloud cover, high cloud cover, medium cloud cover, low cloud cover, near-surface temperature (tas), precipitable water, TOA net SW radiation, TOA outgoing LW, surface downwelling SW, surface upwelling SW, and surface albedo. In the following, we focus on variables for which all five models exhibit a robust agreement in the sign of correlation.

The models' ΔERF show strong negative correlations ($> \sim -0.5$, $p < 0.001$) with the irrigation-induced change in TOA Outgoing Longwave Radiation (LW) at the global scale (Fig.4A), as well as in SAS (Fig.4B) and WCA (Fig.4G). Physically, this is an expected relationship: since ΔERF is defined as the irrigation-induced change in FSNT - FLNT, a reduction in outgoing LW (which decreases FLNT) inherently increases ΔERF if FSNT remains constant. As established in literature, irrigation cools the surface via enhanced latent heat flux and simultaneously increases low-level humidity (Boucher et al., 2004; Mahmood et al., 2014; Thiery et al., 2017). Both processes suppress outgoing LW, as increased water vapor enhances the local greenhouse effect, while a cooler surface emits less thermal radiation (Li et al., 2022). Interestingly, this correlation reverses in CNA and WNA, suggesting that in these regions, other components of the TOA energy balance (likely SW changes) dominate the ΔERF response.

https://doi.org/10.5194/egusphere-2026-4199
Preprint. Discussion started: 22 July 2026

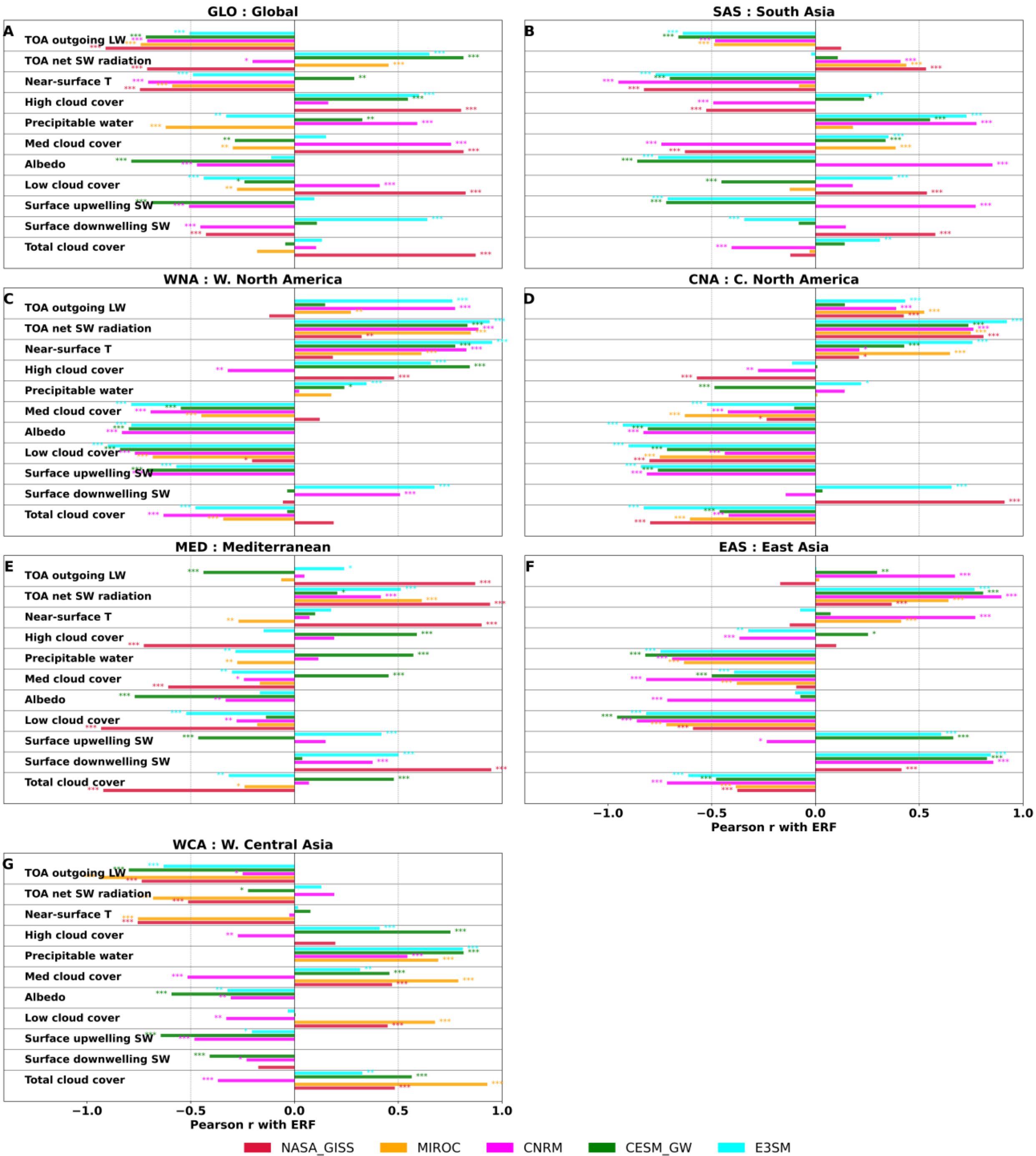

Figure 4: Pearson correlations between 21-year smoothed irrigation-induced Effective Radiative Forcing (ΔERF) and key thermodynamic drivers under all-sky conditions during 1910-2004. Correlation significance levels are denoted by asterisks ($p < 0.05$, ** $p < 0.01$, *** $p < 0.001$).

https://doi.org/10.5194/egusphere-2026-4199
Preprint. Discussion started: 22 July 2026

Similarly to LW, near-surface temperature correlates strongly and negatively with ΔERF in SAS (all models agree on sign). This suggests that irrigation-driven cooling in this region is tightly coupled with a strengthening of the radiative forcing response, primarily dominated by the reduction in outgoing LW. Water vapour acting as a greenhouse gas that traps upwelling LW radiation and radiates it back to the Earth's surface as downward longwave radiation. Although this process tends to increase surface energy input, the increased energy availability appears to be partitioned to latent heat flux through enhanced evapotranspiration, resulting to a net decrease in surface temperature. The high inter-model agreement in SAS compared to the disagreement at the global scale (Fig.4A) indicates that the SAS signal is a robust regional feature that is likely obscured by divergent responses in other regions when averaged globally (Cook et al., 2011). In contrast, models agree on a positive correlation over WNA and CNA, reflecting a regime where higher temperatures coincide with stronger ΔERF, possibly due to dominant SW feedbacks or different evaporative regimes in these semi-arid climates (Singh et al., 2018).

Precipitable water exhibits a positive correlation with ΔERF across SAS, WCA, and WNA ($r \approx 0.6$-0.75). Again, this effect is consistent with physical understanding, where irrigation-induced water vapour increases regional greenhouse trapping, thereby modulating the TOA energy balance (Boucher et al., 2004). Regarding surface albedo, the models show predominantly negative correlations globally and across most regions, indicating that decreases in albedo linked to surface wetting are generally associated with higher ΔERF through enhanced absorption of solar radiation. However, reductions in albedo can also trigger rapid atmospheric adjustments. For example, Laguë et al. (2021) showed that lower land surface albedo increases cloud cover in conjunction with enhanced precipitation, leading to greater reflection of incoming shortwave radiation at the top of the atmosphere and enhanced longwave trapping over land. These competing radiative effects may partially offset one another, thereby moderating the net ΔERF.

Cloud-ΔERF interactions show significant regional variability. Irrigation-induced changes in high cloud cover correlate positively with ΔERF at the global scale, consistent with enhanced longwave trapping by thickening high cloud decks. Conversely, low cloud cover changes correlate negatively with ΔERF in these same regions, indicating that irrigation-induced low cloud thickening acts as a shortwave cooling mechanism that damps the ΔERF (Cheng et al., 2017). However, negative correlations are observed in MED, EAS, and WNA between low (and medium) cloud with ΔERF with agreement in sign across all models. Clouds appear to be a negligible driver of ΔERF variability in SAS, where the models diverge in sign, and where the signal is instead dominated by surface temperature. Overall, the ΔERF of irrigation is a complex metric because irrigation-induced surface cooling often decouples from TOA energy balance shifts (Boucher et al., 2004; Gormley-Gallagher et al., 2022; Mahmood et al., 2014). This regional heterogeneity aligns with findings that local climate responses are determined by the interplay between local energy balance and regional circulation patterns (Cook et al., 2011; de Vrese et al., 2016; Singh et al., 2018).

https://doi.org/10.5194/egusphere-2026-4199
Preprint. Discussion started: 22 July 2026

3.3 Regional and global future annual mean radiation imbalance

As mentioned earlier, unlike the historical period, the future scenario simulations are fully coupled (CMIP-style) runs in which SST responds to the irrigation perturbation; the IRR-NOIRR difference in net TOA radiation therefore reflects both irrigation's forcing and the radiative consequences of the coupled climate response (Section 2.2). We report this quantity as the net TOA radiation imbalance ($\Delta R_{n,TOA}$) and use it here not as a direct extension of the historical ΔERF time series, but as an independent test of whether the regional pattern identified for historical ΔERF, namely the dominance of SAS and WCA and the persistent negative signal over EAS, persists or intensifies under future irrigation and socioeconomic scenarios. Because of the differing experimental design, the magnitudes of $\Delta R_{n,TOA}$ and historical ΔERF (Table 1) should not be compared directly; comparisons across the two periods should be limited to spatial and regional patterns, not absolute values.

Figure 5 shows that $\Delta R_{n,TOA}$, under all-sky conditions, in the future (post-2014), the CESM2-SSP3-7.0 (red) and CESM2-SSP1-2.6 (blue) scenarios diverge only modestly from the historical ΔERF, suggesting that changes in irrigation extent alone may not strongly shift the global energy budget under either pathway, although there is a very small negative trend under SSP126. The future $\Delta R_{n,TOA}$ signal from CESM2 (Fig. 5) shows a similar regional hierarchy to the historical ΔERF, with SAS and WCA exhibiting the largest magnitudes, exceeding 1 W m^{-2} for most of the 2016-2070 period, while the remaining regions remain below 1 W m^{-2} throughout.

In the future period, SSP3-7.0 (higher warming, less efficient irrigation) tends to produce a more positive $\Delta R_{n,TOA}$ compared to SSP1-2.6 over most of the regions, especially over MED, consistent with greater irrigation water demand under a warmer and drier trajectory (Yao et al., 2025b). Yao et al. (2025b) have projected that annual irrigation water withdrawal decreases under SSP1-2.6 but increases under SSP3-7.0, with new irrigation hotspots emerging in Africa. The fact that the SSP370 scenario sustains a stronger positive $\Delta R_{n,TOA}$ in heavily irrigated regions aligns with that trajectory: more water applied means stronger latent heat and moisture feedbacks, maintaining or amplifying the regional radiation imbalance signal into the second half of the 21st century. Under SSP3-7.0, the $\Delta R_{n,TOA}$ signal is projected to be stronger in magnitude than under SSP1-2.6 by 2050-2070 over all regions (Table 1), consistent with higher projected irrigation demand under higher warming and continued agricultural intensification. Under SSP1-2.6, a partial stabilisation or weakening of the $\Delta R_{n,TOA}$ is projected in some models, reflecting reduced irrigation extent under stringent climate mitigation pathways where improved efficiency reduces water application rates. The negative trends over EAS are likely to persist until 2070.

https://doi.org/10.5194/egusphere-2026-4199
Preprint. Discussion started: 22 July 2026

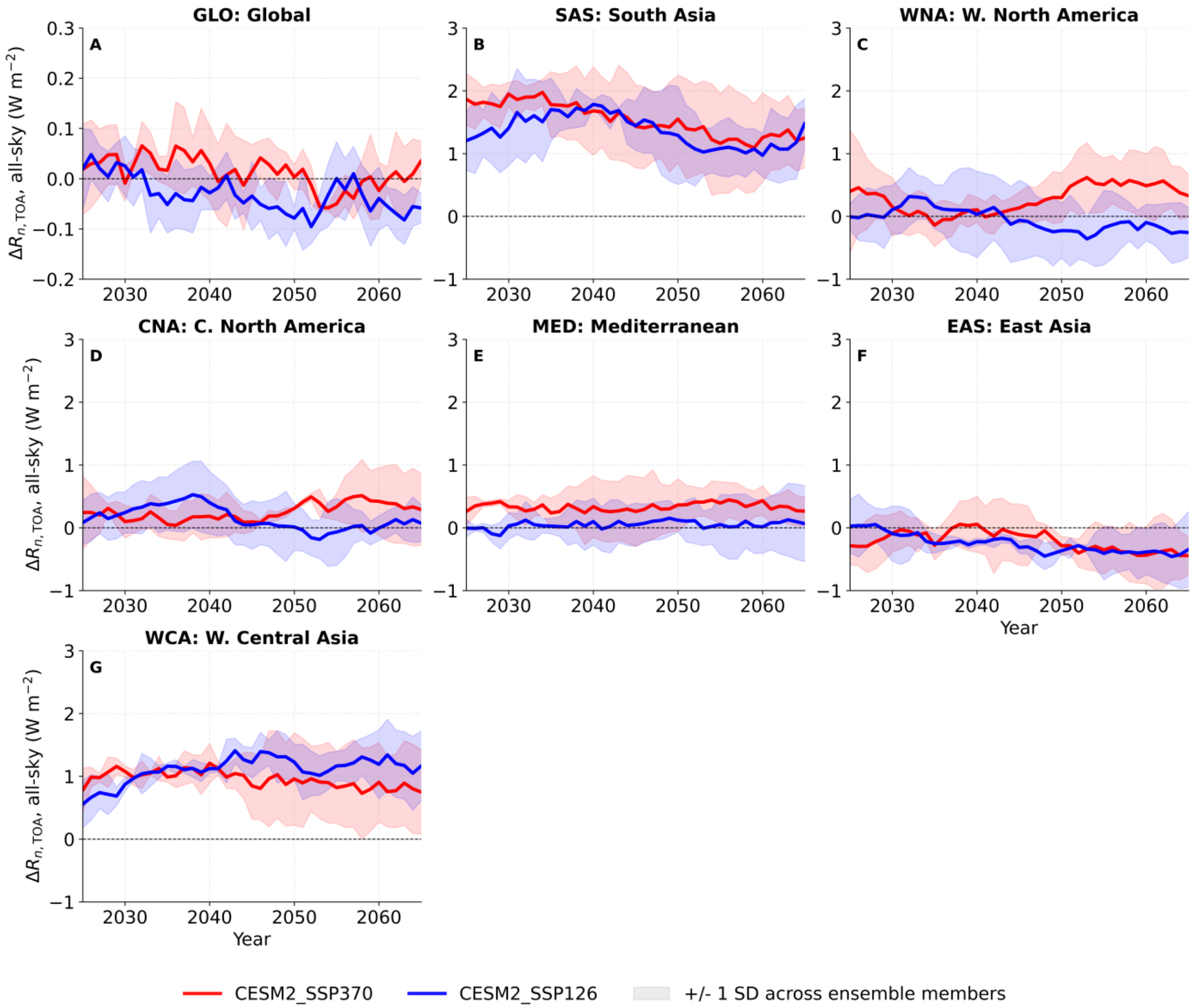

Figure 5: (A-G) Global and regional annual mean radiation imbalance (**$\Delta R_{n,TOA}$**, W m^{-2}) under all-sky conditions from irrigation under future scenarios SSP1-2.6 and SSP3-7.0 (2015-2070). A 21-year Savitzky-Golay smoother is applied. Shading indicates spread across ensemble members (±1 standard deviation).

Compared to the small global values of $\Delta R_{n,TOA}$ under all-sky conditions, with SSP3-7.0 staying mostly slightly positive and SSP1-2.6 dipping more often below zero (Fig.5 A), clear-sky global values (Fig.6 A) are systematically higher than all-sky for both scenarios. This indicates that cloud adjustments pull the global signal down, consistent with what was found for the historical ΔERF, thus clouds are exerting a net negative (cooling) contribution to $\Delta R_{n,TOA}$ in the future runs too.

https://doi.org/10.5194/egusphere-2026-4199
Preprint. Discussion started: 22 July 2026

SAS (Fig.6 B) is the dominant regional signal in all clear-sky conditions (~1-2.5 W/m² vs <1 W/m² elsewhere), with higher clear-sky values (~1.5-2.5+ W/m²) than all-sky for the same years, and the decline over time is similar in shape. In both sky conditions, SSP3-7.0 (red, higher-irrigation-demand) leads SSP1-2.6 (blue) early on, but they cross around 2040-2050, and SSP1-2.6 ends up higher by 2065-2070. A qualitatively similar pattern occurs in WCA, where $\Delta R_{n,TOA}$ rises steadily from ~0.5-0.9 W m^{-2} in 2016 to a plateau of 1-2 W m^{-2} by the 2040s, again with SSP3-7.0 leading initially before the scenarios converge and reverse ordering after approximately 2045. Figs. 5E and 6E show that $\Delta R_{n,TOA}$ over MED has a smaller magnitude, with SSP3-7.0 systematically exceeding SSP1-2.6 throughout most of the simulation period in both sky conditions but remains stable throughout the period. EAS is distinct in showing a sign reversal under clear-sky conditions, with $\Delta R_{n,TOA}$ transitioning from weakly positive to weakly negative after approximately 2030-2040 under both scenarios. Overall, across all regions, clear-sky $\Delta R_{n,TOA}$ is consistently equal to or larger than all-sky $\Delta R_{n,TOA}$, indicating that cloud adjustments exert a systematic damping influence on the $\Delta R_{n,TOA}$ response to irrigation in the future projections, mirroring the all-sky/clear-sky relationship found for the historical ΔERF.

https://doi.org/10.5194/egusphere-2026-4199
Preprint. Discussion started: 22 July 2026

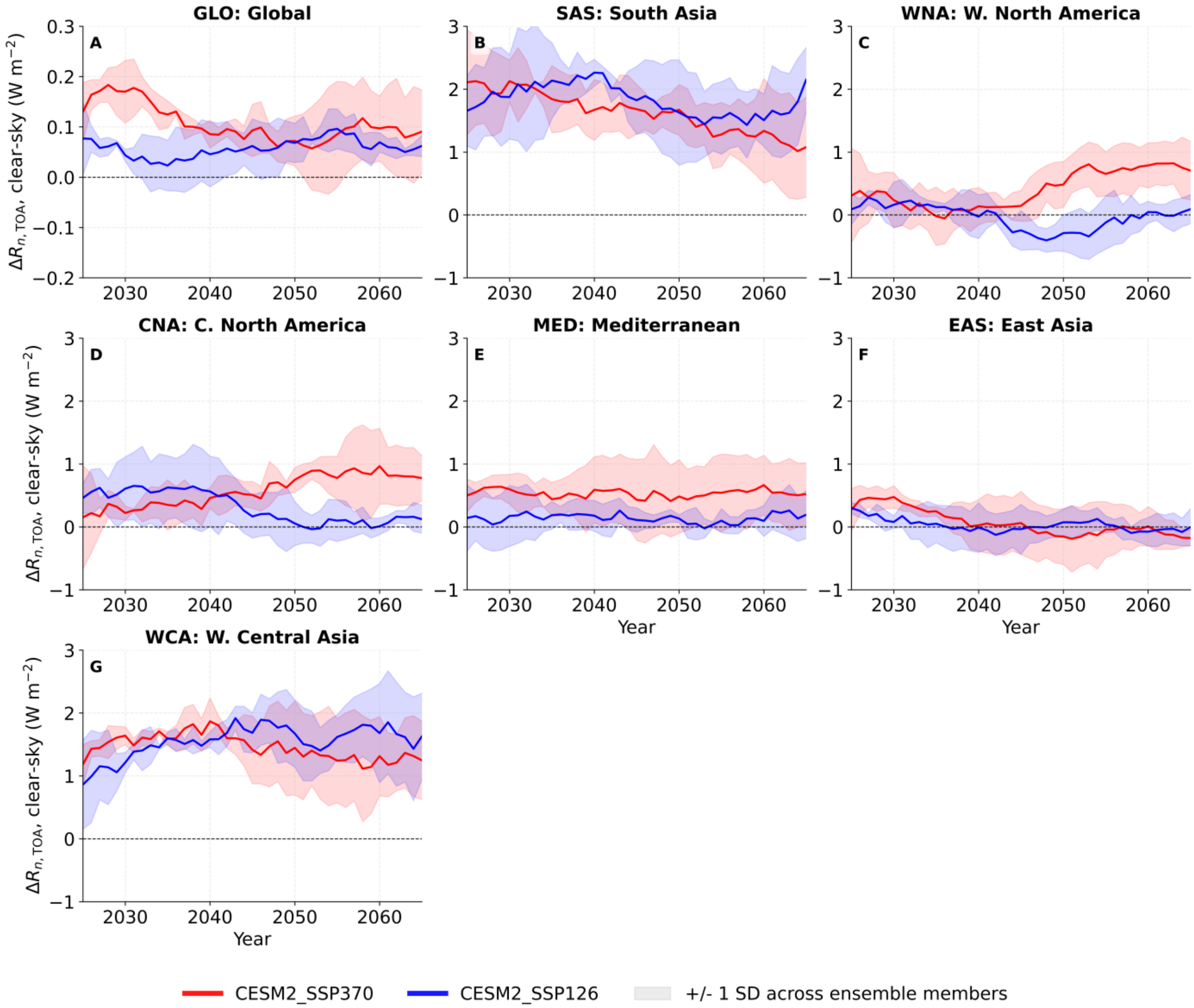

Figure 6: same as Fig.5 but under clear-sky conditions.

Figure 7 shows the spatial distribution of the irrigation-induced radiation imbalance (IRR- NOIRR) under two future SSPs from CESM2, under all-sky (Fig7 A,B) and clear-sky (Fig.7 C,D) conditions, averaged over 2050-2070. The spatial structure of projected future $\Delta R_{n,TOA}$ broadly resembles the historical pattern, but with notable regional shifts. Under SSP3-7.0, the positive $\Delta R_{n,TOA}$ over SAS intensifies relative to the historical mean, while Central Asia and parts of Sub-Saharan Africa show emerging irrigation signals associated with the projected expansion of irrigated area in those regions. Under SSP1-2.6, the $\Delta R_{n,TOA}$ is more muted, particularly over already-irrigated regions where improved irrigation efficiency is projected to

https://doi.org/10.5194/egusphere-2026-4199
Preprint. Discussion started: 22 July 2026

reduce water application rates per unit area. These results suggest that the radiative influence of irrigation in the future is sensitive to both the trajectory of agricultural expansion and the efficiency of water use. Future land-use scenarios should more explicitly represent the evolution of irrigation practices and that climate models should account for irrigation as a climate-relevant land-management forcing. Under all-sky conditions (Fig.7 A,B), the spatial pattern is heterogeneous with both positive and negative anomalies of comparable magnitude scattered across irrigated and non-irrigated regions, particularly over the oceans. SSP3-7.0 shows somewhat stronger positive signals over South Asia and West Central Asia compared to SSP1-2.6, which instead exhibits a large negative anomaly (-3 to -5 W m^{-2}) over the tropical Atlantic and Indian Ocean, an ocean region where no irrigation occurs. This ocean signal is a strong indicator of cloud radiative adjustments driven remotely by irrigation-induced moisture and circulation changes rather than a direct local forcing (Laguë et al., 2022). Under the clear-sky (Fig.7 C,D), over the major irrigated regions including the Indo-Gangetic Plain, WCA, and the MED, a consistent positive $\Delta R_{n,TOA}$ of +1 to +3 W m^{-2} emerges clearly in both scenarios. The ocean anomalies that dominated the all-sky ΔERF (Fig.7 A,B) are almost entirely absent in clear-sky (Fig.7 C,D), confirming they were cloud-mediated responses rather than direct water vapour forcing (Laguë et al., 2021). The clear-sky signal is also more spatially coherent between SSP3-7.0 and SSP1-2.6, with SSP3-7.0 producing somewhat larger positive values over South Asia and Central Asia, consistent with greater irrigation water application under the higher-emission scenario.

Cook et al. (2015) showed that the relative magnitude of the longwave and shortwave processes causes regional increases in energy availability at the TOA over northern India, where the enhanced longwave effect dominates, while over Central Asia and China, the shortwave reductions from enhanced cloud cover drive an overall decline. It seems that this is also true under future conditions: South Asia and West Central Asia are consistently positive in clear-sky ΔERF, while East Asia shows weaker and more mixed signals, consistent with a notable role of cloud-shortwave compensation there. Overall, the total all-sky $\Delta R_{n,TOA}$ from irrigation is not simply the water vapour greenhouse effect. The cloud adjustments can be of comparable or greater magnitude and opposite sign, making the all-sky $\Delta R_{n,TOA}$ highly model- and scenario-dependent. This is consistent with findings from Sherwood et al. (2018), who showed that increases in water vapour greenhouse effect from near-surface emissions (as in irrigation) are partially offset by increases in reflectance from low-level clouds, leading to an effective radiative forcing likely near zero globally but with significant regional structure.

https://doi.org/10.5194/egusphere-2026-4199
Preprint. Discussion started: 22 July 2026

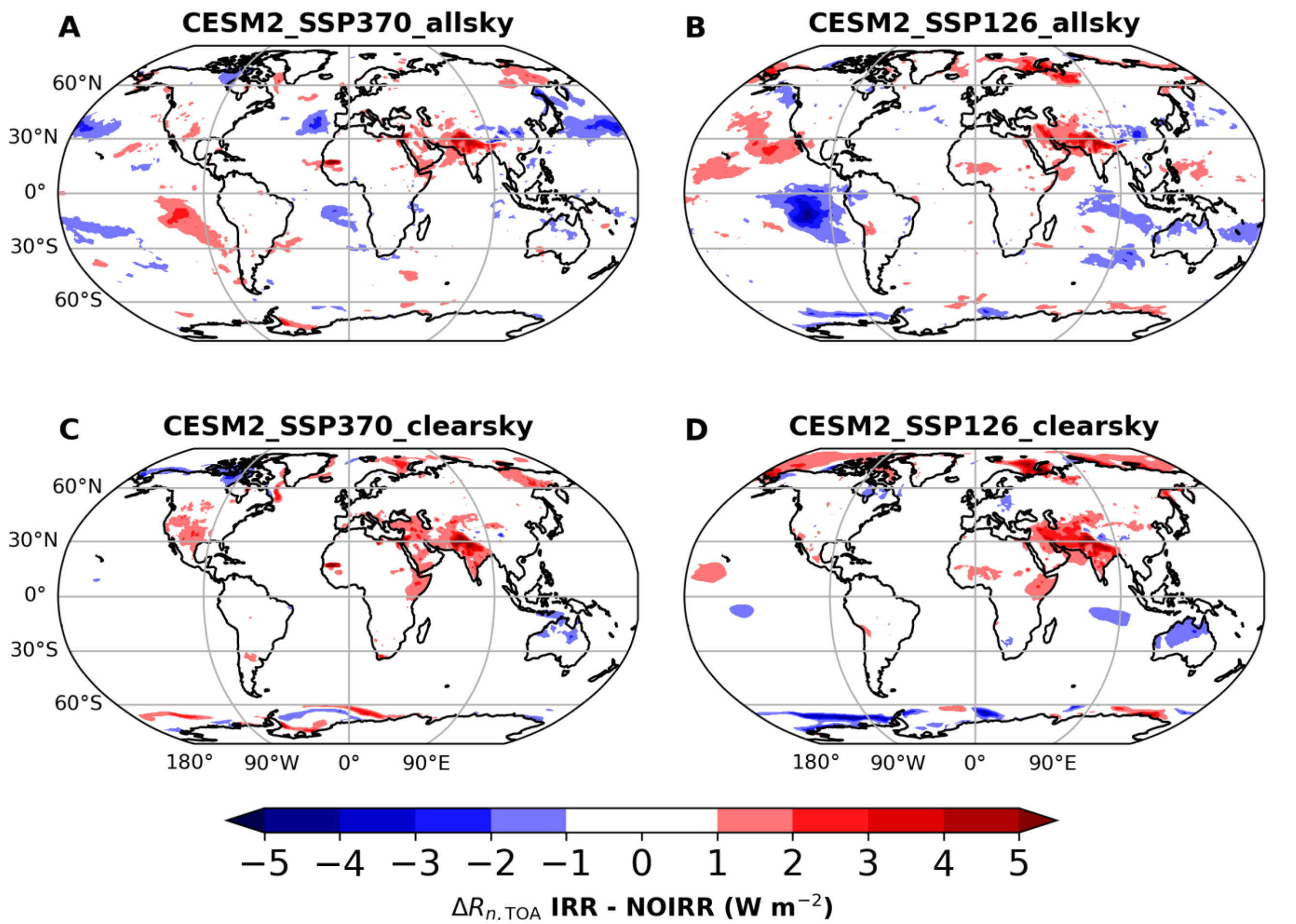

415 Figure 7: As Figure 3, but for the projected 2050-2070 mean of $\Delta R_{n,TOA}$ under SSP1-2.6 (right) and SSP3-7.0 (left) from CESM2.

4. Conclusions

This study provides the first multi-model assessment of irrigation-induced ΔERF using the IRRMIP ensemble, spanning historical (1902-2014) simulations across seven Earth system models. Three main conclusions can be drawn. First, the global mean irrigation ΔERF (all-sky) is positive and small (MMM ≈ 0.023 W m^{-2}) with no clear historical trend, consistent with earlier single-model estimates (Boucher et al., 2004; Cook et al., 2015; Gormley-Gallagher et al., 2022) but with the opposite sign to Sherwood et al. (2018). This small global signal arises largely from a near-cancellation between longwave trapping by irrigation-enhanced atmospheric moisture and shortwave reflection associated with cloud changes and should therefore not be interpreted as evidence of weak regional radiative responses. It is likely affected by a small signal-to-noise ratio,

https://doi.org/10.5194/egusphere-2026-4199
Preprint. Discussion started: 22 July 2026

where forcings of the order of +0.1 W m^{-2} are the threshold for effective detection in AMIP-style experiments (Forster et al., 2016). Second, this global cancellation masks a strong regional structure. South Asia and West Central Asia show model-consistent positive ΔERF reaching 1-5 W m^{-2} locally, concentrated over the Indo-Gangetic Plain, while East Asia shows a persistent negative signal, confirming that irrigation can have substantial local effects. Clear-sky diagnostics confirm that cloud adjustments act as systematic negative feedback that damps the all-sky forcing in most regions and dominate considerably over the noise in the overall ΔERF signal, underscoring that irrigation's radiative footprint cannot be inferred from greenhouse-gas perturbations by atmospheric moisture alone. The driver analysis further shows that ΔERF variability is most strongly associated with variability in outgoing longwave radiation at the global scale and in the most strongly forced regions. Temperature, moisture, and albedo also contribute to explaining ΔERF variability, but their relationships are weaker, reflecting their influence on the radiative response through changes in atmospheric and surface properties. The fact that some relationships (e.g., the sign of the temperature-ΔERF correlation) differ between South Asia and the semi-arid regions of North America and the Mediterranean highlights that no single physical mechanism generalizes across all irrigated regions. Third, the future projections indicate that the $\Delta R_{n,TOA}$ radiation imbalance associated with irrigation is sensitive to the socioeconomic pathway governing irrigation extent and efficiency: SSP3-7.0, which projects higher irrigation water demand, produces a stronger positive $\Delta R_{n,TOA}$ than SSP1-2.6 across the globe by 2070. This suggests that the radiative consequences of irrigation are not fixed but will evolve with both climate trajectory and water-management choices and should therefore be considered explicitly in the land-use components of future climate scenarios.

Several areas for improvement remain and should be explored in future studies: (i) The driver attribution in Section 3.2 is based on only five of the seven IRRMIP models (CNRM, CESM2-GW, NASA-GISS, MIROC, and E3SM), (ii) The future scenario simulations (CESM2 under SSP1-2.6 and SSP3-7.0) are fully coupled (CMIP-style) runs, in contrast to the fixed-SST AMIP configuration used for the historical experiments. As a result, the IRR-NOIRR difference in net TOA radiation for the future period ($\Delta R_{n,TOA}$, Table 1 and Figs 5-7) reflects both the irrigation forcing and the radiative consequences of the coupled SST/circulation response and should not be interpreted as ΔERF in the same sense as the historical values. We retain these coupled-run diagnostics because they offer a preliminary indication of how the net radiative consequences of irrigation may evolve under contrasting socioeconomic pathways, with $\Delta R_{n,TOA}$ generally larger under SSP3-7.0 than SSP1-2.6 across most regions. However, isolating a true future ΔERF would require fixed-SST (AMIP-style) future experiments or a dedicated forcing-feedback decomposition, which are beyond the scope of the present study and are identified here as a priority for future work. (iii) Correlation-based driver attribution does not establish causal direction; several of the candidate drivers (e.g., cloud cover, albedo, water vapor) are themselves rapid adjustments to the same underlying perturbation rather than independent forcings, so the reported relationships should be interpreted as diagnostic of co-variation, not as a decomposition into independent causal pathways. Finally, future work should prioritize expanding the diagnostic output of additional IRRMIP models to enable a more complete multi-model driver attribution, incorporating multiple models into the future-scenario analysis to test the robustness of the SSP-dependent ΔERF strengthening reported here, and developing harmonized historical-future experimental protocols to remove the discontinuities currently introduced by differing irrigation parameterizations and atmosphere-only versus coupled configurations.

Code and data availability

No proprietary software was used. The code used to generate the figures in this paper is available via GitHub: https://github.com/VUB-HYDR.

Supplement link

The link to the supplement will be included by Copernicus, if applicable.

Author contributions

A.A., C.S. and W.T. designed the study. A.A. led the writing of the paper and the preparation of the figures. C.S. performed the initial analysis of the ERF from IRRMIP models. Y.Y and W.T coordinated IRRMIP. K.S.A, M.L, S.M., L.N., L.L., Y.P., Y.S., T.Y. performed the IRRMIP ESM simulations. All co-authors contributed to writing sections and reviewing drafts of the paper.

Competing interests

The contact author has declared that none of the authors has any competing interests.

Disclaimer

Copernicus Publications remains neutral with regard to jurisdictional /claims made in the text, published maps, institutional affiliations, or any other geographical representation in this paper. While Copernicus Publications makes every effort to include appropriate place names, the final responsibility lies with the authors. Views expressed in the text are those of the authors and do not necessarily reflect the views of the publisher.

Acknowledgements

This work was supported by the European Commission Marie Curie Postdoctoral Fellowship grant #101106066 (A.A.). W.T. received funding from the European Research Council (ERC) under the European Union's Horizon Framework research and innovation programme (grant agreement No 101076909; 'LACRIMA' project), and the European Union's Horizon Europe programme (grant agreement No 101295156; 'FUTURA'). T.Y. was supported by the Program for the Advanced Studies of Climate Change Projection (SENTAN, grant number JPMXD0722681344). Y.S. was supported by JSPS KAKENHI (Grant Number 22K14101). The computational resources and services used in this work for the storage and analysis of IRRMIP data were provided by the VSC (Flemish Supercomputer Center), funded by the Research Foundation-Flanders (FWO) and the Flemish Government-department EWI.

Financial support

This work was supported by the European Commission Marie Curie Postdoctoral Fellowship grant #101106066 (A.A.). W.T. received funding from the European Research Council (ERC) under the European Union's Horizon Framework research and innovation programme (grant agreement No 101076909; 'LACRIMA' project), and the European Union's Horizon Europe programme (grant agreement No 101295156; 'FUTURA'). T.Y. was supported by the Program for the Advanced Studies of Climate Change Projection (SENTAN, grant number JPMXD0722681344). Y.S. was supported by JSPS KAKENHI (Grant Number 22K14101). The computational resources and services used in this work for the storage and

https://doi.org/10.5194/egusphere-2026-4199
Preprint. Discussion started: 22 July 2026

analysis of IRRMIP data were provided by the VSC (Flemish Supercomputer Center), funded by the Research Foundation-Flanders (FWO) and the Flemish Government-department EWI.

Review statement

The review statement will be added by Copernicus Publications listing the handling editor as well as all contributing referees according to their status anonymous or identified.

References

Al-Yaari, A., Ducharne, A., Thiery, W., Cheruy, F., Lawrence, D., 2022. The Role of Irrigation Expansion on Historical Climate Change: Insights From CMIP6. https://doi.org/10.1029/2022EF002859

Bellouin, N., Davies, W., Shine, K.P., Quaas, J., Mülmenstädt, J., Forster, P.M., Smith, C., Lee, L., Regayre, L., Brasseur, G., Sudarchikova, N., Bouarar, I., Boucher, O., Myhre, G., 2020. Radiative forcing of climate change from the Copernicus reanalysis of atmospheric composition. Earth Syst. Sci. Data 12, 1649–1677. https://doi.org/10.5194/essd-12-1649-2020

Boucher, O., Myhre, G., Myhre, A., 2004. Direct human influence of irrigation on atmospheric water vapour and climate. Clim. Dyn. 22, 597–603. https://doi.org/10.1007/s00382-004-0402-4

Cheng, W., Moore, J.C., Cao, L., Ji, D., Zhao, L., 2017. Simulated climate effects of desert irrigation geoengineering. Sci. Rep. 7, 46443. https://doi.org/10.1038/srep46443

Cook, B.I., Puma, M.J., Krakauer, N.Y., 2011. Irrigation induced surface cooling in the context of modern and increased greenhouse gas forcing. Clim. Dyn. 37, 1587–1600. https://doi.org/10.1007/s00382-010-0932-x

Cook, B.I., Shukla, S.P., Puma, M.J., Nazarenko, L.S., 2015. Irrigation as an historical climate forcing. Clim. Dyn. 44, 1715–1730. https://doi.org/10.1007/s00382-014-2204-7

de Vrese, P., Hagemann, S., Claussen, M., 2016. Asian irrigation, African rain: Remote impacts of irrigation. Geophys. Res. Lett. 43, 3737–3745. https://doi.org/10.1002/2016GL068146

Döll, P., Fiedler, K., Zhang, J., 2009. Global-scale analysis of river flow alterations due to water withdrawals and reservoirs. Hydrol. Earth Syst. Sci. 13, 2413–2432. https://doi.org/10.5194/hess-13-2413-2009

Forster, P.M., Richardson, T., Maycock, A.C., Smith, C.J., Samset, B.H., Myhre, G., Andrews, T., Pincus, R., Schulz, M., 2016. Recommendations for diagnosing effective radiative forcing from climate models for CMIP6. J. Geophys. Res. Atmos. 121, 12,460-12,475. https://doi.org/10.1002/2016JD025320

Gormley-Gallagher, A.M., Sterl, S., Hirsch, A.L., Seneviratne, S.I., Davin, E.L., Thiery, W., 2022. Agricultural management effects on mean and extreme temperature trends. Earth Syst. Dyn. 13, 419–438. https://doi.org/10.5194/esd-13-419-2022

Hurtt, G.C., Chini, L., Sahajpal, R., Frolking, S., Bodirsky, B.L., Calvin, K., Doelman, J.C., Fisk, J., Fujimori, S., Klein Goldewijk, K., Hasegawa, T., Havlik, P., Heinimann, A., Humpenöder, F., Jungclaus, J., Kaplan, J.O., Kennedy, J., Krisztin, T., Lawrence, D., Lawrence, P., Ma, L., Mertz, O., Pongratz, J., Popp, A., Poulter, B., Riahi, K., Shevliakova, E., Stehfest, E., Thornton, P., Tubiello, F.N., van Vuuren, D.P., Zhang, X., 2020a. Harmonization of global land use change and management for the period 850–2100 (LUH2) for CMIP6. Geosci. Model Dev. 13, 5425–5464. https://doi.org/10.5194/gmd-13-5425-2020

Hurtt, G.C., Chini, L., Sahajpal, R., Frolking, S., Bodirsky, B.L., Calvin, K., Doelman, J.C., Fisk, J., Fujimori, S., Klein Goldewijk, K., Hasegawa, T., Havlik, P., Heinimann, A., Humpenöder, F., Jungclaus, J., Kaplan, J.O., Kennedy, J., Krisztin, T., Lawrence, D., Lawrence, P., Ma, L., Mertz, O., Pongratz, J., Popp, A., Poulter, B., Riahi, K., Shevliakova, E., Stehfest, E., Thornton, P., Tubiello, F.N., van Vuuren, D.P., Zhang, X., 2020b. Harmonization of global land use change and management for the period 850–2100 (LUH2) for CMIP6. Geosci. Model Dev. 13, 5425–5464. https://doi.org/10.5194/gmd-13-5425-2020

Intergovernmental Panel on Climate Change (IPCC) (Ed.), 2023. The Earth's Energy Budget, Climate Feedbacks and Climate Sensitivity, in: Climate Change 2021 – The Physical Science Basis: Working Group I Contribution to the Sixth Assessment Report of the Intergovernmental Panel on Climate Change. Cambridge University Press, Cambridge, pp. 923–1054. https://doi.org/10.1017/9781009157896.009

Intergovernmental Panel on Climate Change (IPCC) (Ed.), 2014. Anthropogenic and Natural Radiative Forcing, in: Climate Change 2013 – The Physical Science Basis: Working Group I Contribution to the Fifth Assessment Report of the

https://doi.org/10.5194/egusphere-2026-4199
Preprint. Discussion started: 22 July 2026

Intergovernmental Panel on Climate Change. Cambridge University Press, Cambridge, pp. 659–740. https://doi.org/10.1017/CBO9781107415324.018

Koll, D.D.B., Cronin, T.W., 2018. Earth's outgoing longwave radiation linear due to H2O greenhouse effect. Proc. Natl. Acad. Sci. 115, 10293–10298. https://doi.org/10.1073/pnas.1809868115

Laguë, M.M., Quetin, G.R., Boos, W.R., 2022. Downwind control of oceanic air by land: the land wake and its sensitivity to CO2. Environ. Res. Lett. 17, 104045. https://doi.org/10.1088/1748-9326/ac9702

Laguë, M.M., Swann, A.L.S., Boos, W.R., 2021. Radiative Feedbacks on Land Surface Change and Associated Tropical Precipitation Shifts. J. Clim. 34, 6651–6672. https://doi.org/10.1175/JCLI-D-20-0883.1

Li, H., Lo, M.-H., Peel, M.C., Ryu, D., Thiery, W., Zhang, Y., 2026. Local and Remote Impacts of Regional Irrigation on Near-Surface Temperature. J. Geophys. Res. Atmos. 131, e2026JD046366. https://doi.org/10.1029/2026JD046366

Li, H., Lo, M.-H., Ryu, D., Peel, M., Zhang, Y., 2022. Possible Increase of Air Temperature by Irrigation. Geophys. Res. Lett. 49, e2022GL100427. https://doi.org/10.1029/2022GL100427

Mahmood, R., Pielke Sr., R.A., Hubbard, K.G., Niyogi, D., Dirmeyer, P.A., McAlpine, C., Carleton, A.M., Hale, R., Gameda, S., Beltrán-Przekurat, A., Baker, B., McNider, R., Legates, D.R., Shepherd, M., Du, J., Blanken, P.D., Frauenfeld, O.W., Nair, U. s., Fall, S., 2014. Land cover changes and their biogeophysical effects on climate. Int. J. Climatol. 34, 929–953. https://doi.org/10.1002/joc.3736

McDermid, S., Nocco, M., Lawston-Parker, P., Keune, J., Pokhrel, Y., Jain, M., Jägermeyr, J., Brocca, L., Massari, C., Jones, A.D., Vahmani, P., Thiery, W., Yao, Y., Bell, A., Chen, L., Dorigo, W., Hanasaki, N., Jasechko, S., Lo, M.-H., Mahmood, R., Mishra, V., Mueller, N.D., Niyogi, D., Rabin, S.S., Sloat, L., Wada, Y., Zappa, L., Chen, F., Cook, B.I., Kim, H., Lombardozzi, D., Polcher, J., Ryu, D., Santanello, J., Satoh, Y., Seneviratne, S., Singh, D., Yokohata, T., 2023. Irrigation in the Earth system. Nat. Rev. Earth Environ. 4, 435–453. https://doi.org/10.1038/s43017-023-00438-5

Mishra, V., Ambika, A.K., Asoka, A., Aadhar, S., Buzan, J., Kumar, R., Huber, M., 2020. Moist heat stress extremes in India enhanced by irrigation. Nat. Geosci. 13, 722–728. https://doi.org/10.1038/s41561-020-00650-8

Mueller, N.D., Rhines, A., Butler, E.E., Ray, D.K., Siebert, S., Holbrook, N.M., Huybers, P., 2017. Global Relationships between Cropland Intensification and Summer Temperature Extremes over the Last 50 Years. J. Clim. 30, 7505–7528. https://doi.org/10.1175/JCLI-D-17-0096.1

Puma, M.J., Cook, B.I., 2010. Effects of irrigation on global climate during the 20th century. J. Geophys. Res. Atmos. 115. https://doi.org/10.1029/2010JD014122

Ramaswamy, V., Collins, W., Haywood, J., Lean, J., Mahowald, N., Myhre, G., Naik, V., Shine, K.P., Soden, B., Stenchikov, G., Storelvmo, T., 2018. Radiative Forcing of Climate: The Historical Evolution of the Radiative Forcing Concept, the Forcing Agents and their Quantification, and Applications. Meteorol. Monogr. 59, 14.1-14.101. https://doi.org/10.1175/AMSMONOGRAPHS-D-19-0001.1

Roy, S.S., Mahmood, R., Niyogi, D., Lei, M., Foster, S.A., Hubbard, K.G., Douglas, E., Pielke Sr., R., 2007. Impacts of the agricultural Green Revolution–induced land use changes on air temperatures in India. J. Geophys. Res. Atmos. 112. https://doi.org/10.1029/2007JD008834

Savitzky, Abraham., Golay, M.J.E., 1964. Smoothing and Differentiation of Data by Simplified Least Squares Procedures. Anal. Chem. 36, 1627–1639. https://doi.org/10.1021/ac60214a047

Seneviratne, S.I., Corti, T., Davin, E.L., Hirschi, M., Jaeger, E.B., Lehner, I., Orlowsky, B., Teuling, A.J., 2010. Investigating soil moisture–climate interactions in a changing climate: A review. Earth-Sci. Rev. 99, 125–161. https://doi.org/10.1016/j.earscirev.2010.02.004

Sharma, A.K., Ganguly, D., Bhattacharya, A., Sarkar, T., Sharma, A., Ghosh, S., Anand, S., Venkataraman, C., Dey, S., 2026. Assessing Aerosol Radiative Forcing and Atmospheric Absorption Over South Asia: A Multi-Model Intercomparison Study. J. Geophys. Res. Atmos. 131, e2025JD044925. https://doi.org/10.1029/2025JD044925

Sherwood, S.C., Bony, S., Boucher, O., Bretherton, C., Forster, P.M., Gregory, J.M., Stevens, B., 2015. Adjustments in the Forcing-Feedback Framework for Understanding Climate Change. Bull. Am. Meteorol. Soc. 96, 217–228. https://doi.org/10.1175/BAMS-D-13-00167.1

Sherwood, S.C., Dixit, V., Salomez, C., 2018. The global warming potential of near-surface emitted water vapour. Environ. Res. Lett. 13, 104006. https://doi.org/10.1088/1748-9326/aae018

https://doi.org/10.5194/egusphere-2026-4199
Preprint. Discussion started: 22 July 2026

Siebert, S., Burke, J., Faures, J.M., Frenken, K., Hoogeveen, J., Döll, P., Portmann, F.T., 2010. Groundwater use for irrigation – a global inventory. Hydrol. Earth Syst. Sci. 14, 1863–1880. https://doi.org/10.5194/hess-14-1863-2010

Siebert, S., Kummu, M., Porkka, M., Döll, P., Ramankutty, N., Scanlon, B.R., 2015. A global data set of the extent of irrigated land from 1900 to 2005. Hydrol. Earth Syst. Sci. 19, 1521–1545. https://doi.org/10.5194/hess-19-1521-2015

Singh, D., McDermid, S.P., Cook, B.I., Puma, M.J., Nazarenko, L., Kelley, M., 2018. Distinct Influences of Land Cover and Land Management on Seasonal Climate. J. Geophys. Res. Atmos. 123, 12,017-12,039. https://doi.org/10.1029/2018JD028874

Thiery, W., Davin, E.L., Lawrence, D.M., Hirsch, A.L., Hauser, M., Seneviratne, S.I., 2017. Present-day irrigation mitigates heat extremes. J. Geophys. Res. Atmos. 122, 1403–1422. https://doi.org/10.1002/2016JD025740

Thiery, W., Visser, A.J., Fischer, E.M., Hauser, M., Hirsch, A.L., Lawrence, D.M., Lejeune, Q., Davin, E.L., Seneviratne, S.I., 2020. Warming of hot extremes alleviated by expanding irrigation. Nat. Commun. 11, 290. https://doi.org/10.1038/s41467-019-14075-4

Tuinenburg, O.A., Hutjes, R.W.A., Jacobs, C.M.J., Kabat, P., 2011. Diagnosis of Local Land–Atmosphere Feedbacks in India. J. Clim. 24, 251–266. https://doi.org/10.1175/2010JCLI3779.1

van Oldenborgh, G.J., Philip, S., Kew, S., van Weele, M., Uhe, P., Otto, F., Singh, R., Pai, I., Cullen, H., AchutaRao, K., 2018. Extreme heat in India and anthropogenic climate change. Nat. Hazards Earth Syst. Sci. 18, 365–381. https://doi.org/10.5194/nhess-18-365-2018

Wu, L., Feng, J., Qin, F., Qiu, Y., 2022. Regional Climate Effects of Irrigation Over Central Asia Using Weather Research and Forecasting Model. J. Geophys. Res. Atmos. 127, e2021JD036210. https://doi.org/10.1029/2021JD036210

Yao, Y., Ducharne, A., Cook, B.I., De Hertog, S.J., Aas, K.S., Arboleda-Obando, P.F., Buzan, J., Colin, J., Costantini, M., Decharme, B., Lawrence, D.M., Lawrence, P., Leung, L.R., Lo, M.-H., Devaraju, N., Wieder, W.R., Wu, R.-J., Zhou, T., Jägermeyr, J., McDermid, S., Pokhrel, Y., Elling, M., Hanasaki, N., Muñoz, P., Nazarenko, L.S., Otta, K., Satoh, Y., Yokohata, T., Jin, L., Wang, X., Mishra, V., Ghosh, S., Thiery, W., 2025a. Impacts of irrigation expansion on moist-heat stress based on IRRMIP results. Nat. Commun. 16, 1045. https://doi.org/10.1038/s41467-025-56356-1

Yao, Y., Satoh, Y., van Maanen, N., Taranu, S., Keune, J., De Hertog, S.J., Lampe, S., Lawrence, D.M., Sacks, W.J., Wada, Y., Ducharne, A., Cook, B.I., Seneviratne, S.I., Liu, L., Buzan, J.R., Jägermeyr, J., Thiery, W., 2025b. Compounding future escalation of emissions- and irrigation-induced increases in humid-heat stress. Nat. Commun. 16, 9326. https://doi.org/10.1038/s41467-025-64375-1

Yao, Y., Thiery, W., Ducharne, A., Cook, B.I., Ding, A., De Hertog, S.J., Sieber, P., Aas, K.S., Arboleda-Obando, P.F., Colin, J., Costantini, M., Decharme, B., Lawrence, D.M., Lawrence, P., Leung, L.R., Lo, M.-H., Devaraju, N., Wu, R.-J., Zhou, T., Jägermeyr, J., McDermid, S.S., Pokhrel, Y., Satoh, Y., Yokohata, T., Gudmundsson, L., Seneviratne, S.I., 2025c. Irrigation-induced land water depletion aggravated by climate change. Nat. Water 3, 1424–1435. https://doi.org/10.1038/s44221-025-00529-1

Yao, Y., Vanderkelen, I., Lombardozzi, D., Swenson, S., Lawrence, D., Jägermeyr, J., Grant, L., Thiery, W., 2022. Implementation and Evaluation of Irrigation Techniques in the Community Land Model. https://doi.org/10.1029/2022MS003074